PCCP

In situ X-ray Spatial Profiling Reveals Uneven Compression of Electrode Assemblies and Steep Lateral Gradients in Lithium-ion Coin Cells

Journal:	*Physical Chemistry Chemical Physics*
Manuscript ID	CP-ART-08-2020-004436.R1
Article Type:	Paper
Date Submitted by the Author:	12-Sep-2020
Complete List of Authors:	Abraham, Daniel; Argonne National Laboratory , Chemical Sciences and Engineering Division Okasinski, John; Argonne National Laboratory, X-Ray Science Division, Advanced Photon Source Shkrob, Ilya; Argonne National Laboratory, Chemical Sciences and Engineering Chuang, Andrew; Argonne National Laboratory, X-ray Sciences Division Rodrigues, Marco ; Argonne National Laboratory, Chemical Science and Engineering Division Raj, Abhi; Princeton University, Department of Electrical Engineering Dees, Dennis; Argonne National Laboratory, Chemical Sciences and Engineering Division

In situ X-ray Spatial Profiling Reveals Uneven Compression of Electrode Assemblies and Steep Lateral Gradients in Lithium-ion Coin Cells

John S. Okasinski,[1] Ilya A. Shkrob,[2] Andrew Chuang,[1] Marco-Tulio Fonseca Rodrigues,[2] Abhi Raj,[2,3] Dennis W. Dees,[2] and Daniel P. Abraham* [2]

[1] X-ray Science Division, Advanced Photon Source, Argonne National Laboratory, Lemont, Illinois 60439, USA

[2] Chemical Sciences and Engineering Division, Argonne National Laboratory, Lemont, Illinois, 60439, USA

[3] Department of Electrical Engineering, Princeton University, Princeton, New Jersey 08544, USA

* Corresponding author: E-mail: abraham@anl.gov

Keywords: energy dispersive X-Ray diffraction, radiography, spacer deformation, radial inhomogeneity, electrochemical modeling, separator porosity

Abstract

Coin cells are used extensively as test devices in battery research for evaluation of new materials and optimization of cycling protocols. In this study, *in situ* X-ray diffraction profilometry is used to characterize spatial distribution of the active materials, lithiation, and phase distribution in electrodes of NCM523/graphite coin cells. The X-ray data indicate uneven areal compression of the electrode assembly in such cells, which we trace to a specific design feature that leads to elastic deformation of a metal spacer. Steep lithiation gradients observed in the electrodes imply radially-dependent resistivity, for which uneven compression of the separator is a likely cause. Electrochemical model calculations suggest that variable porosity of the polymer separator would account for the salient features of spatial profiles observed in these coin cells.

Graphical summary

In situ X-ray diffraction profilometry reveals radially nonuniform compression of the electrode assembly leading to large lateral heterogeneity of lithium intercalation and plating in the standard Li-ion coin cells in fast charge regimes.

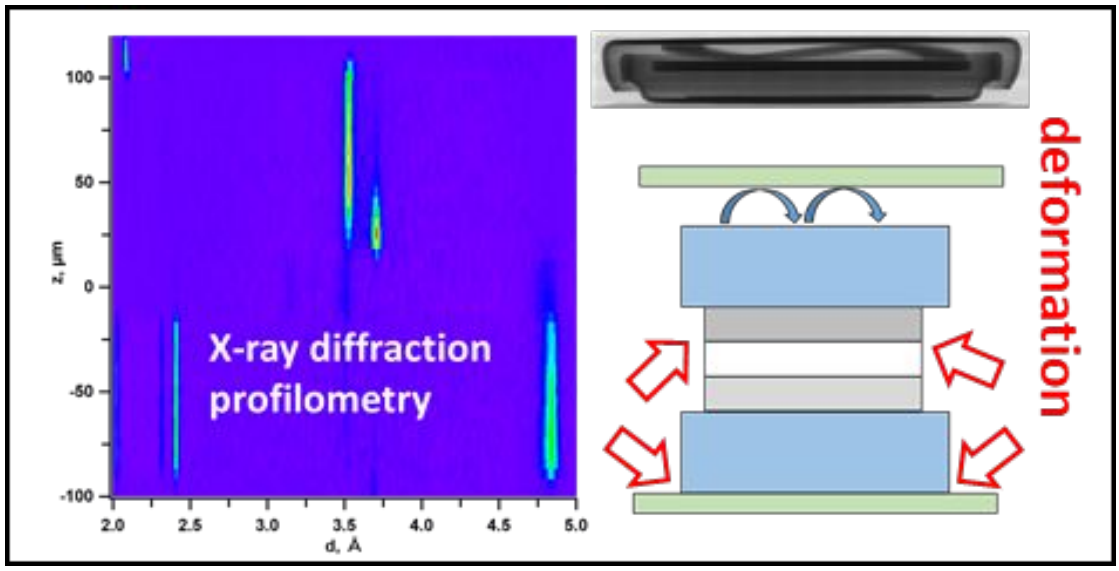

Introduction

Due to their affordability, ease of use, and robust design, coin cells are the most frequently used test devices for research and development in the battery sciences. [1-3] In these cells, flat electrodes sandwich a microporous separator infused with a liquid electrolyte. [4] This assembly is pressed together by two stainless steel (SS) spacers loaded from the top by a wave spring as shown in Figure 1a and inset Table 1. [5] The assembly is housed inside a SS case that is crimp sealed through a gasket. In these cells, the electrode aspect ratio can be as high as 100:1, providing a uniform electric field. The design mitigates concerns with electric and heat conductivity in the leads, and there is sufficient internal volume to accommodate gases generated during electrode-electrolyte reactions. The spring loading and thick SS spacers provide compression and alignment of the electrodes.

We have been using coin cells and energy dispersive X-ray diffraction (EDXRD) to study lithiation gradients that develop in lithium-ion cell electrodes during slow (< C/10) and fast (> 1C) cycling. [6, 7] In this method, a collimated beam of wide spectrum X-rays slices the cell, and the X-rays scattered from the cell are analyzed spectrally, revealing the diffraction patterns of crystalline ordered phases in the electrodes. [6-8] This method can also be used in combination with computed tomography to study individual particles in the matrix. [9, 10] The positions and amplitudes of the diffraction peaks depend on the lithium content of the active materials, allowing *in situ* profiling with ~ 2-5 μm precision. In the course of these studies, we noted strong inhomogeneity both along the radial direction (in the *xy* plane of the laboratory frame) and across the electrode thickness (which is the *z*-axis of this frame); see Figure 1a. This observation has major consequences, as such inhomogeneity can affect the current flow causing large lithium concentration gradients in the electrodes. [11-13] Parasitic reactions along these gradients accelerate localized aging of the cell materials. [14] Furthermore, such inhomogeneity makes it harder to predict cell life, as such forecasts are based on electrochemical models that typically assume lateral uniformity. [15]

In this study, we provide detailed X-ray diffraction profilometry of the electrodes in coin cells. We show that there is radial deformation in the electrode assembly and that this deformation causes pinching of the porous separator. The extent of deformation is examined for various electrode and spacer configurations in the cell. Electrochemical modeling simulations indicate that variable porosity, resulting from the non-uniform separator compression, can contribute to the

radially inhomogeneous lithium distribution observed in the solid electrodes. This awareness is important for battery researchers interpreting data from fast charge and discharge cycles, as the effects of nonuniform separator compression become significant at high rates.

Animations, tables, and figures that supplement information provided in this text are contained in the Supporting Information: these have the designator "S", as in Figure S1.

Methods

The positive and negative electrodes used in this study contain NCM523 oxide ($Li_{1.03}(Ni_{0.5}Co_{0.2}Mn_{0.3})_{0.97}O_2$) and graphite (Gr), respectively, both of them ~70 μm thick; see Table 2. [16] These electrodes were fabricated by casting slurries onto a 10 μm thick copper foil for the Gr anode and 20 μm thick aluminum foil for the NCM523 cathode, using a coater at the Cell Analysis, Modeling and Prototyping (CAMP) facility at Argonne. After drying of the solvent, the electrodes were calendered to obtain uniform thickness. Before cell assembly, all components were dried in a heated vacuum oven. The cells contain 40 μL electrolyte (1.2 M $LiPF_6$ dissolved in a 3:7 w/w solvent mixture of ethylene carbonate and ethyl methyl carbonate) filling pores of the electrodes and a Celgard 2320 separator. This 20-μm-thick separator is a trilayer membrane composed of two layers of β-nucleated polypropylene on the outside and polyethylene on the inside; ~ 1 μm^3 microscopic slits are created by biaxial stretching of the material. [17]

Standard gasket-sealed CR2032 style stainless steel (SS) coin cells from Hohsen Corp. containing 1.58 cm^2 round electrodes were used for cell assembly. This cell is Ø20 mm x 3.2 mm thick with an inner height of 2.57 mm. In the standard assembly (Figures 1a to 1c), a SS spring with n=3 waves per turn presses the electrode assembly between two Ø15.5 mm x 0.5 mm SS spacer disks. The spring has the following dimensions: outer diameter D_{out} of 15 mm, inner diameter D_{in} of 10.6 mm, free height of 1.4 mm, and material thickness t of 0.25 mm. The spring contacts the cap of the coin cell (Figure 1a) pressing on the top spacer, while the bottom spacer directly contacts the can. The deflection Δ of the spring in a sealed cell, obtained from cell radiographs such as in Figure 1a, is 0.27 mm, which corresponds to ~16% compression. The spring constant can be estimated from these data using formulas given below in the Results section. Alternative configurations (see Table 1 in Figure 1b) included thick or thin aluminum spacers that

were used (in lieu of the SS spacers) to reduce attenuation of diffracted X-rays exiting the cell. The thick Al spacers, Ø16 mm x 1 mm, were from Hohsen, whereas the thin Al spacers, Ø15.4 mm x 0.41 mm, were fabricated in our laboratory. Some cells were configured with the cathode on top and anode on the bottom; in others, the order was reversed as indicated in Table 1. The spring was not used in some configurations; instead, compression of the electrode assembly was achieved with the use of additional spacers (see cell-2 in Table 1 and Figure S1a).

Before X-ray studies, the cells underwent two formation cycles at a C/10 rate and a slow additional cycle at a C/25 rate (3.0-4.1 V, 30 °C) before being fully discharged and held at 3.0 V. After X-ray examination in this fully discharged state, the cells were charged under various conditions and allowed to rest. For selected cells in Table 1, Table 3 gives parameters for this galvanostatic charge, including C-rates, capacities at a slow discharge before the charge cycle, terminal charge capacity, and the estimate x for anode lithiation from this charge capacity (referenced to the theoretical capacity of graphite). Note that in multiphase materials such as lithiated graphite, Li^+ ion gradients persist almost indefinitely as phase boundaries serve as barriers to the Li^+ ion diffusion. This persistence makes it possible to map the phase and lithiation gradients in much detail without concern for their temporal stability.

The energy dispersive X-ray diffraction setup at beamline 6BM-A of the Advanced Photon Source at Argonne National Laboratory was used in all experiments. The beam from the synchrotron bending magnet was collimated to a rectangular 2 mm x 10 μm beam that impinged on the cell parallel to the base. An energy-resolving germanium detector placed at a fixed angle $2\theta \approx 2.287°$ in the vertical plane was used to collect the diffracted photons. During the experiment, motorized stages translate the cell radially (the y-axis) or in the perpendicular direction (the z-axis) as illustrated in Figure 1a. The X-ray beam and electrode assembly are aligned using radiography and z-profiled in steps of 2 μm at 10-15 equidistant y-position across the cell diameter. The diffracted spectrum is converted to the d-domain, where the spacing $d(\lambda)$ between crystal planes is calculated from the Bragg equation, $2dsin\theta = \lambda$.

Results and discussion

Electrode curvature from X-ray profiles.

As seen from the false color map of EDXRD spectra in Figure 2 and animated Figure S2, the electrodes, the polymer separator, and the metal current collectors all give strong diffraction peaks in the regions specified in Table 4. The separator diffraction peaks, arising from the high degree of crystalline order in the polymer lamellae, partially overlap with diffraction peaks from lithiated graphite. The diffraction peaks from the current collectors also interfere with signals from the electrodes.

The various peaks were integrated after subtracting the background. The corresponding integrals were corrected for relative intensity and peak overlap. In particular, the LiC_6 integral was corrected to remove overlapping signals from the separator. The LiC_{12} integral was corrected to take into account different scattering cross-section for this phase vs. the LiC_6 phase (see ref. [6]) After these corrections, the phase-weighted lithium content x_k per C_6 for each LiC_{6k} phase was found from $x_k = {k}^{-1}I_k/\sum_k I_k$, where I_k is the normalized integral proportional to the volume fraction of the k-th phase; the total lithiation $x = \sum_k \langle x_k \rangle$. To estimate lithium content of the cathode, the two strongest (003) and (101) peaks were indexed assuming a hexagonal cell with the lattice parameters a=b and c. The d-spacing for centroids is given by $d = c/3$ and $d = \left(4c^{-2}/3 + a^{-2}\right)^{-1/2}$, respectively, from which the unit cell constants a and c can be estimated; the lithium content $\check{x}$ of the oxide-cathode was obtained from a heuristic equation ${a}/{a_0} = 1 - {\alpha}/{\left[1 + exp\left(\left(\check{x} - x_0\right)/\Delta x\right)\right]}$, where $a_0 = 2.886$ Å, $\alpha = 2.5\text{x}10^{-3}$, $x_0 = 0.781$, and $\Delta x = 0.158$, which holds for $\check{x}$ < 0.2 (at lower Li contents, the lattice irreversibly collapses). [18] This equation was obtained by fitting high-resolution crystallographic data (the hexagonal cell was accurately indexed using 6-8 peaks) to the lithium content $\check{x}$, estimated from electrochemical measurements at slow charge (< C/10 rate).

To obtain the material profiles along the z-axis, $\sum_k I_k$ for the Li_xC_6 peaks and the integral of the oxide (101) peak were plotted vs. the depth z of the beam centroid in the electrode assembly. The stronger (003) peaks were not used due to their partial overlap with the separator and Al peaks. Typical profiles are shown in Figure 3 and animated Figure S3. The profiles are the least squares

fitted with gated polynomials convoluted with the Gaussian function representing the X-ray beam profile in the material as explained in the caption to Figure S3. The gate gives the hard electrode edges, which are plotted as a function of the radial position *y* in Figures 4 and 5. Each cell has a different configuration as detailed in Table 1. Figures 4 and 5 together show that, regardless of the electrode stacking sequence in Figure 1a, the bottom electrode is always more strongly curved than the top one. As seen by plotting the gap between the electrodes (Figure 6), this gap is smaller near the edge and greater at the center.

Given the porosity of the separator (~40% before it swells in the electrolyte), Figure 6 suggests that the pores could be partially closed near the edges, which would distort currents flowing through the cell. Even a small (4-6 μm) compression of the separator can be effectual, as the polymer membrane consists of a soft polypropylene layer on a rigid polyethylene inner layer, added for mechanical stability; only this soft layer needs to be blocked to increase the local resistance. As described later, variable pore closure in the separator can account for the radial inhomogeneity observed in the electrodes.

Pressure induced deformations.

Both the radiographs and measurements using a depth gauge indicate that the bottom can of the coin cell is slightly concave. Consequently, at the center there is a small gap (< 15-30 μm) between the bottom of the spacer and the concave wall of the can; this gap varies from cell to cell. When the simply-supported bottom spacer becomes uniformly loaded, it deforms slightly, becoming concave, and the bottom (but not the top) electrode follows the surface of this spacer, also becoming concave (Figures 4 to 6). The top spacer and the top electrode both remain almost flat: the top can is not deformed because the pressure during crimping is absorbed by the spring. The bottom spacer deforms because the entire load on it is supported at the contact line. We focus on this deformation as it translates into a variable gap between the electrodes and affects electrochemical behavior of the cell.

Given a sufficiently high load, a simply supported plate will deflect, so the only question is whether the spring load is sufficient to cause the observed deflection. For cell-1, our measurement using a dial gauge gave an estimate of 18 μm for the gap between the can wall and the flat bottom spacer. Thus, there is sufficient room to accommodate the deflection. We

approximate the spacer by a thin Kirchhoff-Love plate of thickness h and the contact radius R that is simply supported at the edge under a uniformly distributed load q. [19] The material in the spacer has the Young's modulus E and the Poisson's ratio ν. Introducing the reduced coordinate $\rho = y/R$, the z-axis deflection $z(\rho)$ of the circular plate with the boundary condition $z(1)=0$ is given by the Germain-Laplace formula

$$z(\rho) = \delta \frac{2(3+\nu)(1-\rho^2) - (1+\nu)(1-\rho^4)}{5+\nu} \quad (1)$$

where $\delta = \frac{qR^4(5+\nu)}{64D(1+\nu)}$ is the maximum deflection at $\rho = 0$ and the flexural rigidity $D = \frac{Eh^3}{12(1-\nu^2)}$. For ν≈1/3,

$$\frac{\delta}{R} \approx \frac{2q}{3E}\left(\frac{R}{h}\right)^3 \quad (2)$$

To obtain the estimates of δ in Table 1, we fit to the gap between the electrodes

$$\zeta(y) = \zeta_0 + y\,tan\vartheta + z(y/R), \quad (3)$$

where ζ_0 is the gap width at $y = R$, ϑ is the wedge angle, and the third term is given by eq. 1 (Figures 6a and 6b show such least-squares fits). From the fit parameters, the average gap width ζ across the diameter is given by $\langle\zeta\rangle = \zeta_0 + \frac{8\delta(6+\nu)}{15(5+\nu)}$, from which the maximum variation $\delta/\langle\zeta\rangle$ given in the last column of Table 1 was calculated.

For stainless steel, E ≈ 190 GPa and ν ≈ 0.265, while for aluminum E ≈ 69 GPa and ν ≈ 0.334; the difference in stiffness of these materials accounts for a greater δ for Al spacers (Table 1 and Figure 5). Using eq. 1, we estimate that for the standard stainless steel spacer (h=0.5 mm, R=7.09 mm) δ≈10 μm would be equivalent to the distributed load q ≈ 0.14 MPa. To estimate the load, the spring constant is given by $K = \varrho E t^3/D_m^2$, where $D_m = (D_{out} + D_{in})/2$ is the mean diameter, the dimensionless spring constant $\varrho \approx \frac{\mu n^4 D_{out}}{k\ D_{in}}$, $\mu = (D_{out} - D_{in})/(D_{out} + D_{in})$, and the multiple wave factor k=3.88 for n=2-4. [20] Using the parameters given in the Experimental, these formulae give K≈110 N/mm (at our request, the manufacturer shared test data suggesting estimates between 60 and 117 N/mm), which is equivalent to a distributed load $q = K\Delta/\pi R^2$ of 0.185 MPa.

The two estimates point to the same load range; i.e. *compression of the spring is sufficient to deform the bottom spacer to the observed extent*.

To reduce deflection, the cell design was modified as detailed in Table 1. Because the deflection δ decreases as h^{-3} (see eq. 2), a thicker Al spacer ($h = 1$ mm) was used, with or without a stainless steel ring-shaped shim beneath the bottom spacer (Figure 5). In both cases the spring became over compressed, resulting in an increased load and corresponding increase in deformation. Replacing the SS spring with four SS spacers (Figure S1a) made the deflection δ smaller (Table 1 and Figure 4), but it was difficult to avoid wedging of the electrodes (i.e., large angles ϑ in eq. 3). The smallest deflection of 3.5±0.6 μm was obtained using a 100 μm thick ring-shaped SS shim in combination with a 0.41 mm thick Al spacer at the bottom of the cell (Figure S1b), as shown in Figures 5a and 6b. However, as seen from Table 1, none of these changes allowed us to obtain $\delta/\langle\zeta\rangle < 15\%$.

Radial inhomogeneity.

In the charged cells, there are lithiation and phase gradients in addition to the material density gradients. As expected, only LiC_6 and LiC_{12} phases were observed in the lithiated anode of charged cells. The z-profile of these phases is nonuniform (see Figure 7 for the center section of cell-1), with the LiC_6 phase prevalent near the separator and the LiC_{12} phase prevalent near the Cu current collector. Additional examples are shown in Figures S4 and S5, which contain animated z-scans of the anode LiC_x phases and cathode-oxide along the radial direction.

As known from mathematical physics, a smooth profile $x(\xi)$ can be approximated by a sum over the orthogonal polynomials of ξ, where ξ is the reduced depth of the electrode measured from the separator, that varies between 0 and 1. Familiar examples of such series include the H atom radial wavefunctions (the exponentially weighted Laguerre polynomials) and the oscillator wavefunctions (the Hermite polynomials) in quantum mechanics. The choice of these orthogonal polynomials is dictated by the boundary conditions for the partial differential equations of the second order; here we tacitly assume that Li^+ ion transfer can be described by a system of such equations, of which the diffusion equation is an example. As the lithium fluxes become zero at the current collectors, this uniquely defines these orthogonal polynomials as the Legendre polynomials

$P_{2n}(\xi)$ of the even order $2n$, for which $P'_{2n}(1) = 0$. Thus, we assume $x(\xi) \approx \sum_{n=0} u_n P_{2n}(\xi)$, where u_n are the time-dependent weights.

Using the orthogonality of these Legendre polynomials, the average and standard deviation for $x(\xi)$ are given by $u_0 = \langle x \rangle_z$ and $\sigma^2 = \left\langle (x - \langle x \rangle_z)^2 \right\rangle_z = \sum_{n>0} u_n^2/(2n+1)$, respectively. As the absolute weights $|u_n|$ rapidly decrease with *n*, for most part only the u_1 coefficient before $P_2(\xi) = (3\xi^2 - 1)/2$ needs be considered, so the *z*-coordinate average u_0 and the standard deviation $\sigma \approx u_1/\sqrt{5}$ are sufficient to characterize the *z*-axis inhomogeneity. Consequently, in the *yz*-scans, these two quantities are calculated numerically from the lithiation profiles and plotted vs. the radial position *y* to characterize the lateral inhomogeneity.

Figures 8a and 8b show the average u_0 and the standard deviation σ for LiC_6 and LiC_{12} vs. *y*, for cell-1 and cell-2. These profiles can be divided into two regions: (i) the flat top central region and (ii) the edge regions, where the average and standard deviation for the anode materials change rapidly. This non-uniformity persisted even after the cells were at rest for several hours. The cathode's lithium content varies little even in these edge regions (see Figure 8a), suggesting smoothing of lithium concentration gradients in the absence of current. In the anode, the fraction of LiC_6 decreases and the fraction of LiC_{12} increases considerably from the central region towards the edges. While this behavior was observed in all cells, other features varied with the state of charge (see Table 3). For example, in cell-2 (Figure 8b), *σ increases* towards the edges, whereas in cell-1 (Figure 8a) the opposite is observed. Below, we will show that differences between the cells arise from the dynamics of $LiC_{12} \rightarrow LiC_6$ phase transition and the extent of anode lithiation.

In theory, current density should increase towards the edges, causing faster charging. In a cell with the constant electrode gap $\zeta \ll R$, the increase in current density $\Delta j(R) = j(R) - j_\infty$ at the edge is given by [21] $\Delta j(R) = j_\infty/4w$, where j_∞ is the current density far from the edge. The Wagner number $w = \kappa/\zeta \left(d\eta_{int}/di\right)$, where κ is the electrolyte conductivity (~ 10 mS/cm), η_{int} is the Li intercalation overpotential and *i* is the reaction current density given by a linearized Butler-Volmer equation, so that $d\eta_{int}/di = kT/\alpha i_0 e$, where α is the charge transfer coefficient, i_0 is the exchange current, kT is the thermal energy, and *e* is the elementary charge. In our case, $\alpha \approx 0.5$ and $i_0 \approx 40$ μA/cm^2 for the intercalation into graphite, [16, 22] so $w \sim 5\text{x}10^3$. Therefore, the increase in current density is small and, as suggested by plots in ref. [21] and our calculations, limited to a

narrow outer band of thickness $\sim\zeta$. It is seen that this thin-rim edge effect *cannot* account for our observations.

A plausible explanation for the behavior observed in Figure 8 would be a greater resistivity near the electrode edge that decreases the current and causes slower lithiation through this region. During fast charge, this higher resistivity would not only lower the Li intercalation current, but also lower the anode surface potential η_a (the difference between the electrolyte potential and the anode across the interphase), which equals the reaction overpotential for Li plating. [17] Hence, Li plating in the edge regions would be more facile compared to the central regions of the round electrode. Post-mortem images of anodes extracted from fast-charged cells in Figure S6 do reveal a ring of lithium deposits near (but not at) the electrode edge. Such an effect is expected: variable resistance across the gap between the electrodes should affect all reactions occurring on the graphite electrode. There are other reports in the literature suggesting lateral inhomogeneity of Li plating in other types of cells. [23]

Modeling.

The observation of curvature in the electrodes implies that the separator experiences a higher level of compression towards the edges, which can create nonuniform ion currents. To gain additional insight, we used the electrochemical model introduced and described in refs. [16, 22, 24] which considers lithiated graphite as a triphasic system that includes dilute LiC_x phases ($x \leq 1/3$), LiC_{12}, and LiC_6. In this model, the idealized cell is laterally infinite. Using this model, we inquired how the porosity ϵ of the separator would affect cell polarization. To this end, we calculated the anode lithiation x at the attainment of $\eta_a = 0$ (which is the thermodynamic Li plating condition) during a constant rate charge, and plotted this quantity as a function of ϵ (assuming that the tortuosity changes as $\tau = \epsilon^{-1/2}$); see Figure 9. The greater the C-rate, the more gradual the change with increasing porosity. For lower charge rates, the cell polarization increases abruptly when ϵ approaches 0.10-0.15, while the variation in ϵ is largely inconsequential for ϵ between 0.2 to 0.4. This weak dependence accounts for the flat top central region: unless the C-rate is very high, the decrease in separator porosity ϵ needs to be considerable for any effect to be observed. This peculiarity also explains the difficulty of recognizing the problem while cycling at low C-rates (for which the coin cells have been designed).

Including the multiple phase dynamics *and* realistic electrode geometry was prohibitive computationally, and to account for the variable separator porosity, a simplified single-phase model was used. In this model, both electrodes are treated as solid solutions, and the particles of active material have several discrete layers (in our standard model, the intraparticle diffusion of Li^+ ions is continuous, so the number of layers is potentially infinite). [2, 25] Kinetic equations describing Li^+ ion transfer between these discrete layers approximates the continuous diffusion. [25]

By design, this single-phase model cannot yield persistent gradients, which arise from phase boundaries in the graphite and particle boundaries in the oxide. However, one can compute the Li concentration gradients as the current flows during and immediately after charge. To this end we modeled a coin cell as a flat cylindrically symmetric cell of radius R with the constant gap between the electrodes. It was assumed that all lithium concentration gradients vanish at $y = R$, and the separator porosity varied as $\epsilon(\rho) = \epsilon_0(1 - \Xi\rho^2)$, where ρ is the reduced radial coordinate, ϵ_0 is the porosity at the center of the cell (~0.4), and $0 \leq \Xi \leq 1$ is the compression (~0.75). Figure 10 shows the lithiation map across the electrodes obtained at the end of 6C charge (at which the cell voltage reaches 4.5 V and the capacity reaches 2.3 mAh/cm^2) and the computed u_0 and σ plotted vs. y; the animations in Figure S7, panels a and b show the charge progress in time. We used the high charge rate as the single-phase model underestimates the gradients due to their rapid dissipation by diffusion even as the cell is being charged. For the anode, both the average lithiation u_0 and the standard deviation σ exhibit the flat top profiles seen in Figure 8; other features are also qualitatively similar. The curvature of σ in the edge-regions changes from negative to positive as lithiation progresses over time (see animated Figure S7). We remind the reader that cell-1 (Figures 8a) has lower anode lithiation x than cell-2 (Table 3 and Figure 8b). Our calculation suggests that the shape difference in σ for these two cells can be from differences in the anode lithiation (more on that below).

In Figures 10c and S7c we show the Li plating current ($\propto c^{\alpha}|\eta_a|$, where c is the Li^+ concentration in the electrolyte). Our computation assumes that the exchange current for the reaction is too small to compete with the Li intercalation, so one does not need to include Li plating into the mass balance. At the end of charge, the overpotential η_a is negative both on the surface and in the bulk; i.e., the Li plating can occur throughout the porous anode matrix. At all times, the plating current is maximum near the edge, but *not at the edge*; i.e. the plated lithium would form a ring. Thus, the model qualitatively reproduces the ring-like Li plating (Figure S6), further

solidifying the link between the variable resistivity of the separator and the observed lateral inhomogeneity.

To re-introduce phase dynamics, we modified our original (three phase) LiC_x model to include periodicity in the *y*-direction. This allowed us to introduce variable porosity without unduly increasing the computation complexity. The results of 3C charging of this periodic cell is presented in animated Figures S8 and S9. These calculations, by showing phase composition of the anode, indicate that the transition in the slope of σ in the outer region coincides with the stage of charge when LiC_6 replaces the LiC_{12} phase across the cell. This succession of LiC_x phases occurs in the central regions faster than it does near the edge. Similar negative-to-positive changes in σ are predicted to occur during other phase transitions, with the growing phases having σ(*y*) pointing up near the edges and the receding phases pointing down in the same region. In Figure 10, this transformation is still in progress, which is why the slope for σ changes from positive to negative immediately next to the edge. While this planar periodic cell is only an approximation to the cylindrically symmetric cell, the same applies to the cylindrical cell, as it is a natural consequence of phase dynamics in a cell with variable lateral resistance.

Thus, taking into account the experimental observations and modeling results, the connection between spacer deformation, electrode overpotential and C-rates can be summarized as follows. The spacer deformation introduces radial variation of pressure on the electrode assembly and especially on the microporous separator, whose pores are filled with ionically conducting electrolyte. Due to the partial pore closure, this leads to radially dependent resistance across the separator. When the C-rates are high and the currents are strong, there is an iR term associated with this resistance which changes the overpotentials. This overpotential can be sufficiently large in localized areas, so that Li plating would occur in lieu of Li intercalation into the graphite particles.

Conclusions

We use the standard 2032-type coin cells for *in situ* and *operando* studies of electrodes in Li-ion cells cycled at various C-rates. *In situ* X-ray diffraction profilometry was used to characterize the distribution of active materials, phases, and lithiation in cells before and after charge. Our examinations reveal that there is a small gap between the flat bottom spacer and the concave wall of the cell can, so the spacer is simply supported at the edge where it contacts the

reinforced can wall. Under load, this spacer deforms and becomes concave. The bottom electrode follows this curvature, while the top electrode remains relatively flat; this causes nonuniform compression of the electrode assembly. The porous separator is pinched near the edge and dilated at the cell center. Electrochemical model simulations suggest that a decrease in separator porosity caused by this pinching can account for the observed patterns of heterogeneity in the lithium intercalation and plating currents. This compression is inconsequential at low rates, but becomes increasingly problematic at charge rates exceeding 1C, leading to localized lithium plating near, but slightly away, from the electrode edges.

Of the various cell assembly configurations, the addition of a stainless steel shim below the bottom spacer reduced its deflection but could not prevent it completely. A design modification, to mitigate curvature of the bottom electrode, is thickening and flattening of the cell can. This change would ensure that the spacer does not deform the can as it presses on the wall when loaded. While this modification may increase weight, this increase could be acceptable for cells used as test devices in research projects.

Electronic Supporting Information

The supporting information includes a PDF file containing supporting tables and a PowerPoint file with supporting figures and animations that show radiographs, scanning profiles, and experimental and computed phase and lithium distributions.

Conflicts of interest

The authors declare no financial competing interests.

Acknowledgement

This research used resources of the Advanced Photon Source, a U.S. Department of Energy (DOE) Office of Science User Facility, operated for the DOE Office of Basic Energy Science by Argonne National Laboratory (Argonne) under Contract No. DE-AC02-06CH11357. IAS and DPA are grateful for support from Argonne's Laboratory Directed Research & Development (LDRD) program. MTFR and DD acknowledge support from DOE's Vehicle Technologies Office. AR acknowledges support from DOE's Office of Science Graduate Student Research (SCGSR) program administered by the Oak Ridge Institute for Science and Education for the DOE under contract number DE-SC0014664. The electrodes examined in this study were produced at the U.S.

Department of Energy's CAMP (Cell Analysis, Modeling and Prototyping) Facility at Argonne. The CAMP Facility is fully supported by DOE's Vehicle Technologies Office. The submitted manuscript has been created by UChicago Argonne, LLC, Operator of Argonne National Laboratory ("Argonne"). Argonne, a U.S. Department of Energy Office of Science laboratory, is operated under Contract No. DE-AC02-06CH11357. The U.S. Government retains for itself, and others acting on its behalf, a paid-up nonexclusive, irrevocable worldwide license in said article to reproduce, prepare derivative works, distribute copies to the public, and perform publicly and display publicly, by or on behalf of the Government.

Table 2. Cell materials.

Positive Electrode (1.58 cm^2 area)	**Negative Electrode (1.58 cm^2 area)**
90 wt% NCM523 (Toda America)	91.8 wt% Superior Graphite (SLC1506T)
5 wt% C45 (Timcal)	2 wt% C45 (Timcal) + 0.2 wt% oxalic acid
5 wt% PVdF binder (Solvay 5130)	6 wt% PVdF binder (KF-9300 Kureha)
18.6 mg/cm^2 loading density - coating	9.9 mg/cm^2 loading density - coating
16.8 mg/cm^2 loading density - active/oxide	9.1 mg/cm^2 loading density - active/graphite
35.4% electrode porosity	34.5% electrode porosity
71-µm-thick composite coating	70-µm-thick composite coating
20-µm-thick Al current collector	10-µm-thick Cu current collector
Separator: Celgard 2320 20-µm-thick, 40% porosity, trilayer Polypropylene/polyethylene/polypropylene	**Electrolyte**: 1.2 M $LiPF_6$ in 3:7 w/w ethylene carbonate: ethyl methyl carbonate (Tomiyama)

Table 3. Capacity and charging conditions for selected cells in Table 1.

Cell	**C/10 discharge capacity, mAh/cm^2**	**Charge current, mA/cm^2**	**Charge rate**	**Cell capacity after charge, mAh/cm^2**	**Estimated anode-averaged graphite lithiation, x**
1	2.52	2.247	1.50C	1.482	0.59
2	2.37	2.247	1.06C	2.119	0.89
8	2.33	0.197	C/12.3	2.43	1.0

Table 4. *d*-Space regions of interest for determination of the relevant species from the corresponding integrals.

Species	**d_{min}, Å**	**d_{max}, Å**
Graphite and dilute LiC_x solutions	3.300	3.430
LiC_{12}	3.500	3.618
LiC_6	3.618	3.775
Cu (111)	2.050	2.200
separator-1	4.630	5.063
separator-2	3.980	4.350
separator-3	3.590	3.880
NCM523 (003)	4.670	5.050

Figures with captions.

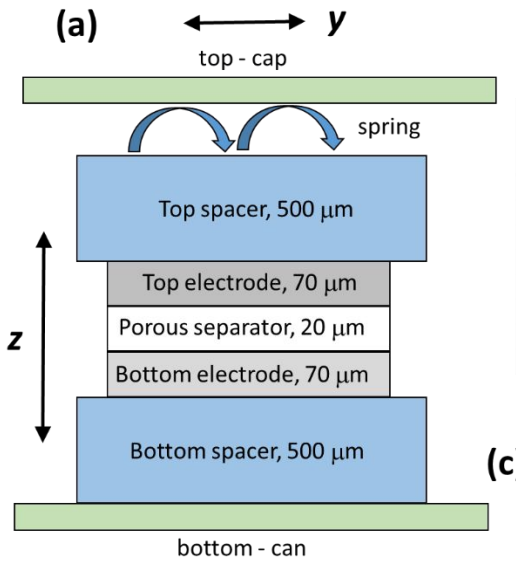

(b) Table 1: Coin Cell Configurations and Deflections δ at the Center of the Bottom Electrode

Cell	Spring loaded	Bottom Shim	Top electrode	Bottom electrode	bottom spacer	bottom spacer material	δ , μm	$\frac{\delta}{\langle\zeta\rangle}$, %
1	x		cathode	anode	A	steel	10.8±0.9	30
2			cathode	anode	A	steel	3.9±0.6	16
3	x		anode	cathode	A	steel	6.1±1.0	21
4			anode	cathode	A	steel	6.2±1.2	27
5	x		anode	cathode	B	Al	15.8±1.1	44
6	x		anode	cathode	C	Al	13.0±1.2	44
7	x	x	anode	cathode	C	Al	14.2±2.3	42
8	x	x	anode	cathode	B	Al	3.5±0.6	15

(c)

Figure 1. *Panel a* gives a schematic of the coin cell, with the nomenclature adopted in this study. Typical thicknesses of the various components are indicated in the plot. The arrows indicate the laboratory frame axes. In Table 1 in *Panel b*, the SS bottom shim is 100 μm thick with an outer diameter of 12 mm and an inner diameter of 6 mm, spacer A is stainless steel (h=0.5 mm), spacer B is aluminum (h=0.41 mm), spacer C is aluminum (h=1.0 mm); the last column in the table gives the ratio of the maximum deflection at the center (δ) to the mean gap width $\langle\zeta\rangle$ between the electrode across the cell diameter. *Panel c* gives the X-ray radiograph of spring-loaded cell-1. All spring-loaded cells had a top SS spacer; the cells that were not spring loaded had a stack of four standard SS spacers on the top.

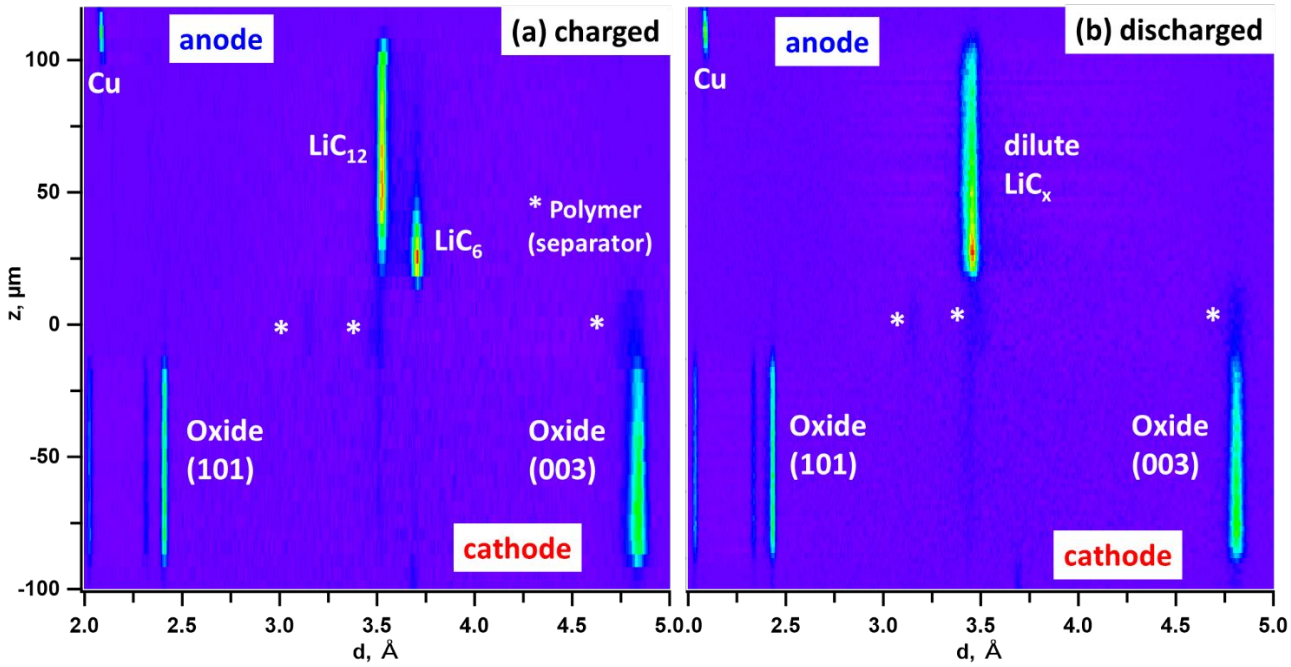

Figure 2. The false color representation of background corrected EDXRD spectra for (a) charged and (b) discharged cell-1 shown in the *d*-space with the vertical axis giving the depth *z*. The colors in the map are arranged in the rainbow order; the zero corresponds to the violet and the highest values correspond to the red. The electrode assembly was scanned from the top to the bottom, with the cathode at the top, see Figure 1a. In the anode, the Bragg peaks from the copper current collector and highly-lithiated graphite phases (panel a) or dilute LiC_x phases (panel b) are seen. In the cathode, two strong peaks from the hexagonal NCM523 oxide are observed. Note the strong transverse heterogeneity in the *z*-profiles for the LiC_x phases compared to the oxide. Also seen in the gap between the two electrodes are the three Bragg peaks from the lamellae in the polymer separator filling this gap. This *z*-scan was obtained at the center of the round cell, see also Figure 3a.

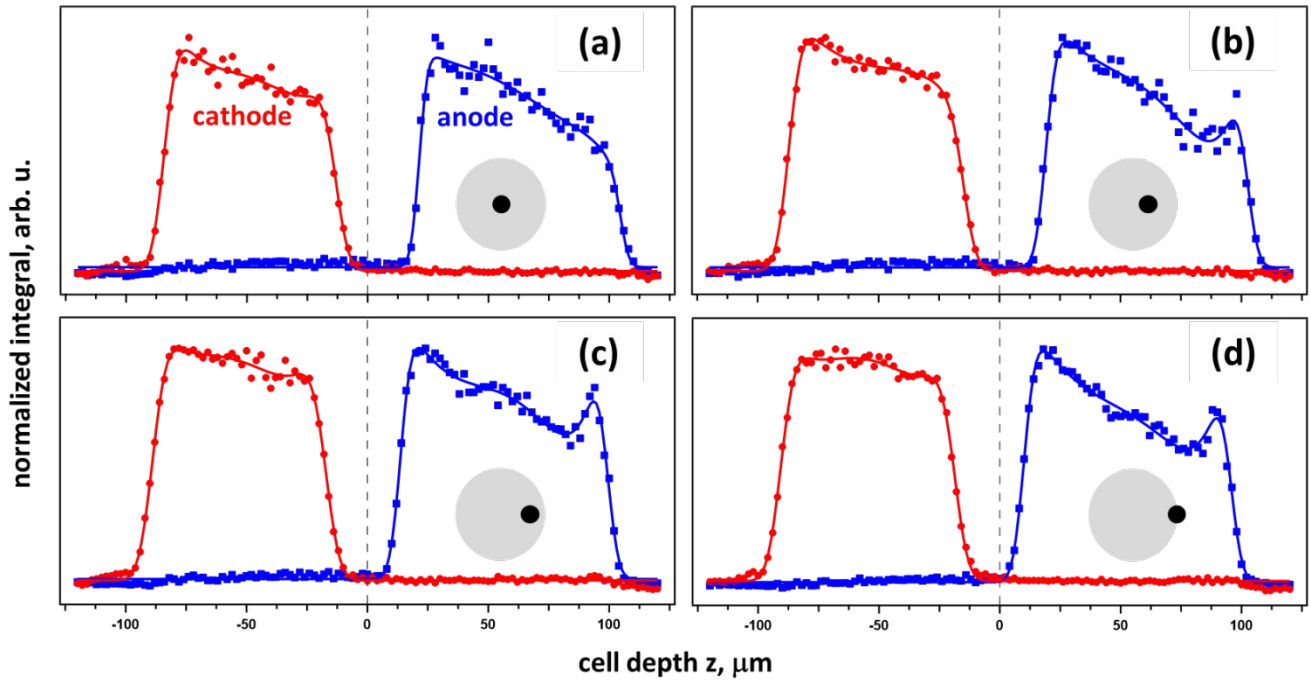

Figure 3. Selected *z*-scans of discharged cell-1 obtained at the radial position *y* of (a) 0, (b) 2, (c) 5, and (d) 7 mm with respect to the cell center. The electrode assembly was *z*-scanned from the top to the bottom. The spatial resolution of the *z*-scan is 2 microns but the hard edges are detected by fitting with resolution better than 0.5 microns. The symbols are the normalized integrals of the oxide cathode (*red*) and graphite anode (*blue*) EDXRD peaks, and the solid lines are gated polynomial convoluted with the beam profile. The insets show lateral positions of the X-ray beam with regard to the electrode assembly. The "horns" seen in the material distribution profiles for the graphite anode are due to preferential orientation and densification of graphite flakes due to calendering of the electrode. See also animated Figure S3.

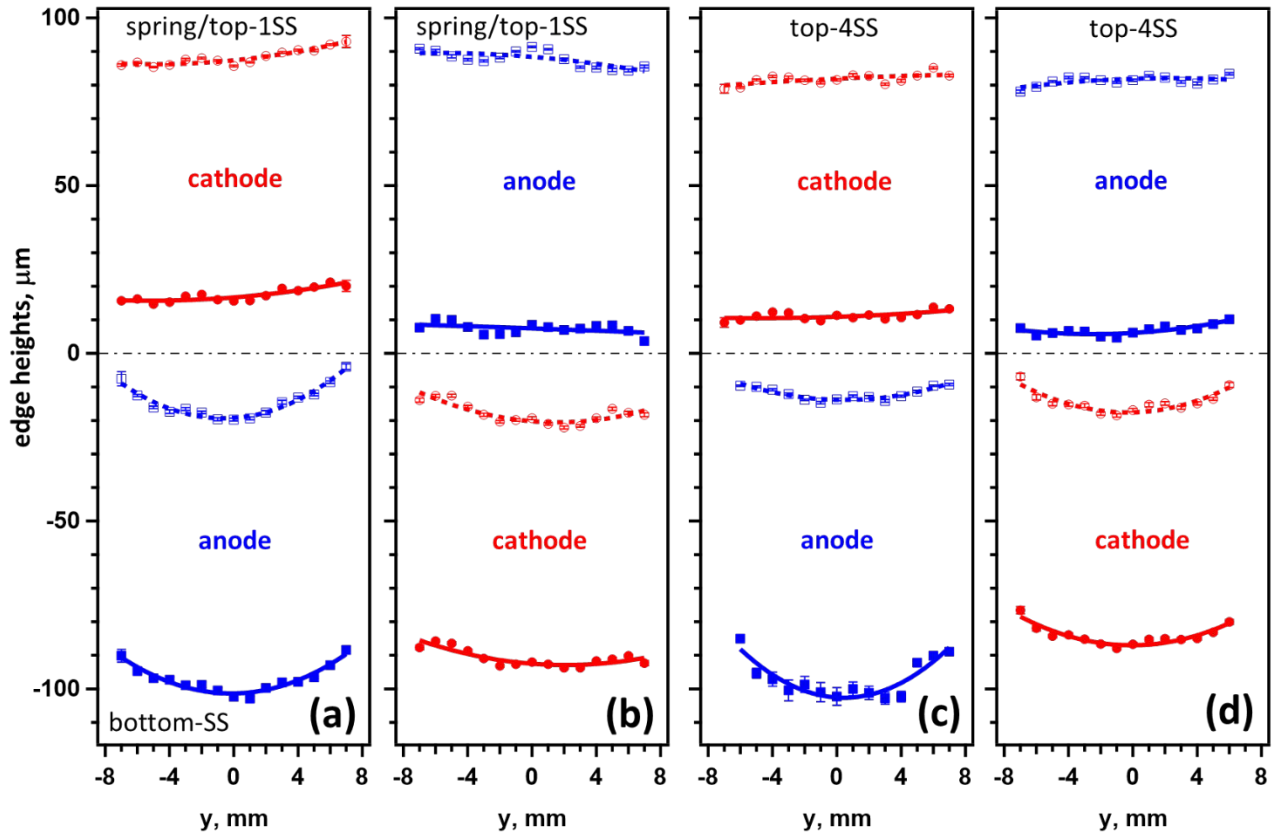

Figure 4. The symbols show hard edge heights of the electrodes measured from the bottom and plotted vs. the radial position *y* of the X-ray beam for (a) cell-1, (b) cell-3, (c) cell-2, and (d) cell-4. All four cells have a single SS spacer at the bottom. Cell-2 and cell-4 have four SS spacers stacked at the top, while cell-1 and cell-3 are spring loaded and have a single SS spacer at the top. The vertical bars in the plots give uncertainties in the edge positions for each measurement, and the solid lines are linear or quadratic fits. In some plots one can see misalignment of the electrode assembly with respect to the vertical axis of the laboratory frame. This misalignment is the same for both electrodes, and it can be subtracted away.

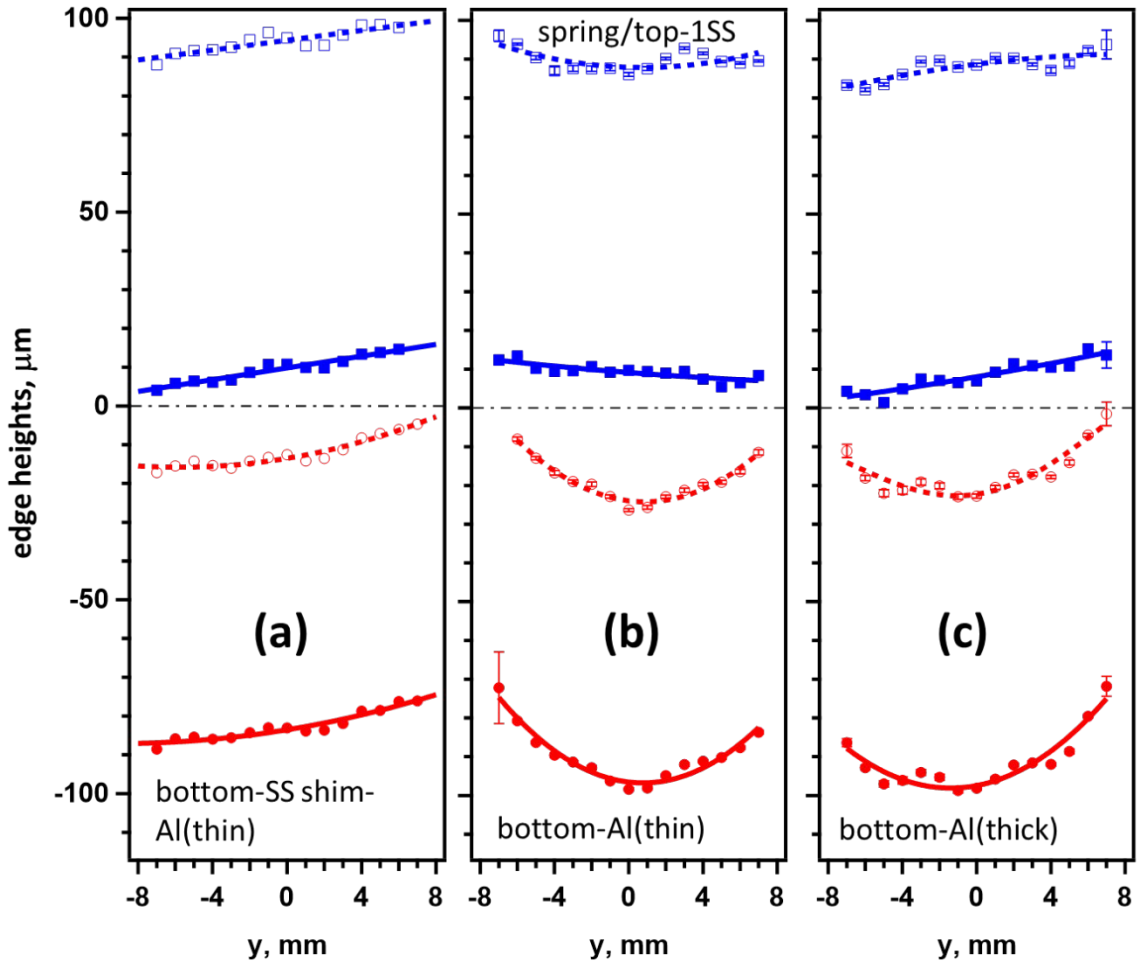

Figure 5. Like Figure 4 for (a) cell-8, (b) cell-5 and (c) cell-6 with aluminum spacers at the bottom to minimize attenuation of the diffracted X-rays. These cells are spring loaded using a single SS spacer at the top. The blue and red symbols and lines are for the anode and cathode, respectively. Cell-8 includes a 100 µm thick ring-shaped SS shim at the bottom, see Figure S1b. The aluminum spacers are either thin (410 µm) or thick (1 mm). The vertical bars are the standard deviations for the edge positions.

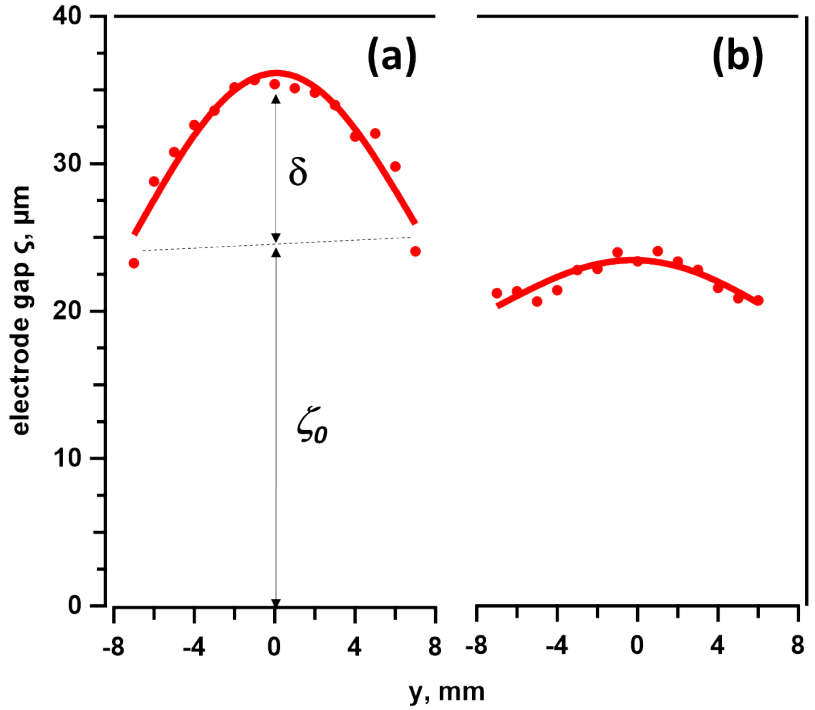

Figure 6. The red filled circles are for the electrode gap ζ in (a) cell-1 and (b) cell-8 (see Table 1) plotted vs. the radial coordinate y. The red lines are least squares fits to eq. 1. The dashed line in panel a indicates slight wedging of the electrodes. The vertical arrows indicate the constant offset ζ_0 and the deflection δ at the center of the cell which are given in Table 1. As evident from the figure, radial deformation of the electrode assembly is much larger in cell-1 than in cell-8.

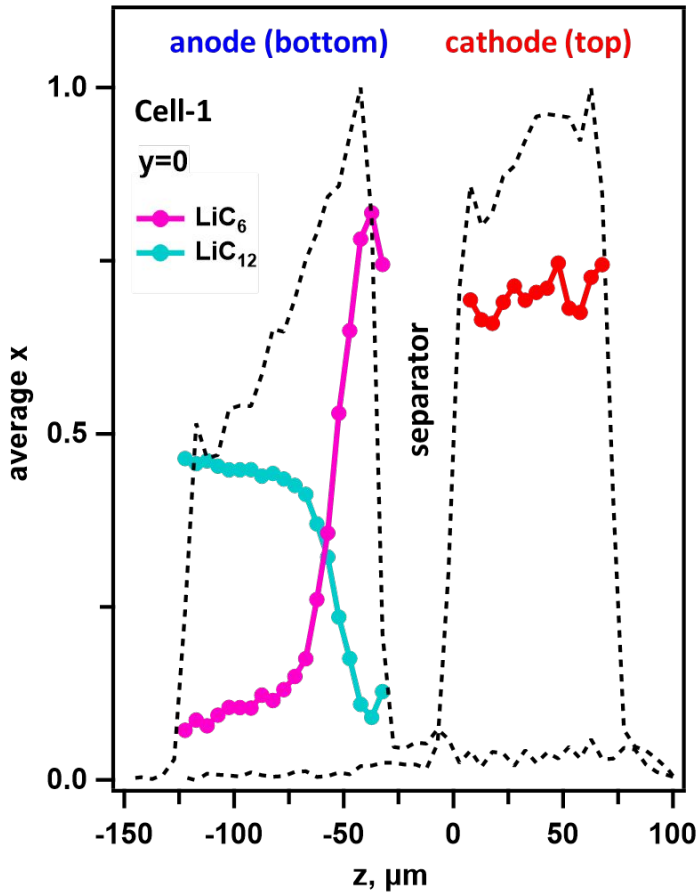

Figure 7. An example of the lithiation profiles obtained from the transverse *z*-scan at *y*=0 for charged cell-1 in Table 1; also see animations in Figure S5. The dashed lines are the active material profiles, the red is for the cathode, and the magenta and cyan are for the LiC_6 and LiC_{12} phases, respectively (other LiC_x dilute phases are not observed at this stage of lithiation). See Figure 2a for the false color map also showing this *z*-axis inhomogeneity. While the Li concentration gradient in the cathode was too small for our analysis, the gradients in the lithiated graphite are steep and can be quantified. See Figure 8a for the *y*-plot of the average and the standard deviation.

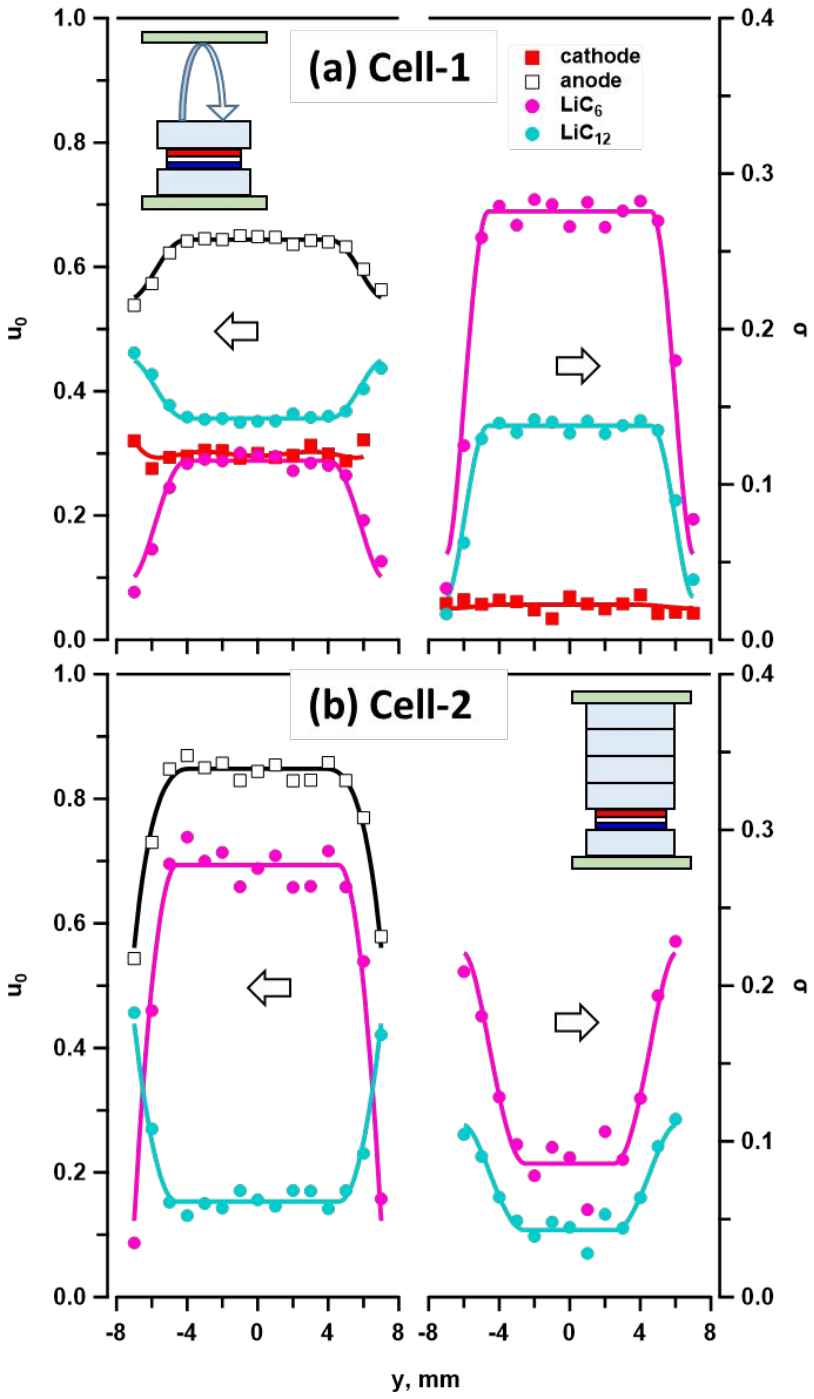

Figure 8. Two examples of the radial *y*-profiles showing variation of the average lithiation u_0 (*to the left*) and the standard deviation σ (*to the right*) for graphite electrode in (a) cell-1 and (b) cell-2 across their diameters (see Tables 1 and S2). In panel a, the cathode's Li content is also shown (*red squares*). The average end-of-charge anode lithiation, estimated from the electrochemistry data, are ~0.6 for cell-1 (panel a) and ~0.9 for cell-2 (panel b). The symbols show lithium contents of the oxide-cathode in red and the graphite-anode in black; for the latter, the contributions from the LiC_6 (*magenta*) and LiC_{12} (*cyan*) phases are also shown. Schematics of cell assemblies are included in the insets.

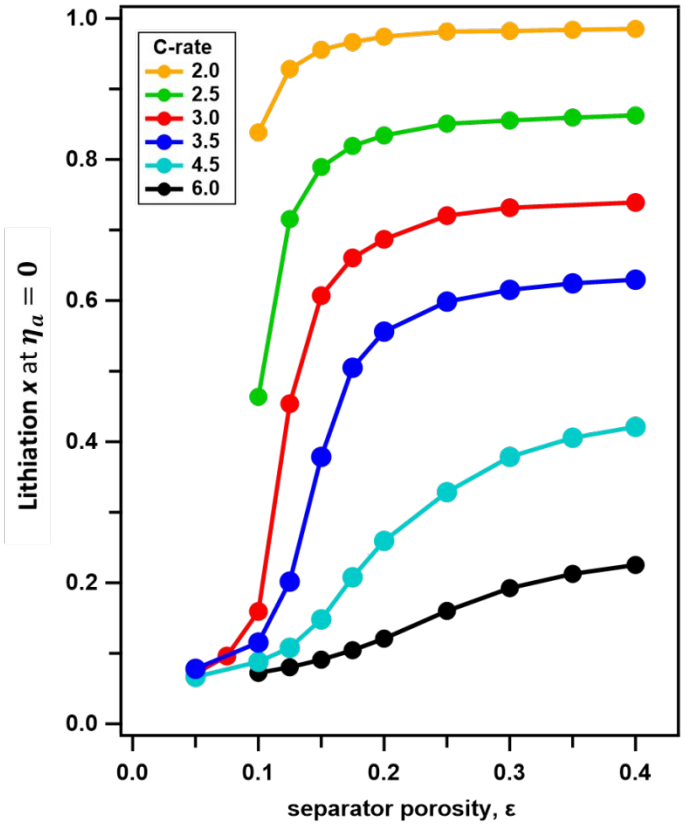

Figure 9. Computed critical lithiation (the ratio x of the terminal and full specific capacities) during galvanostatic charge at the moment when the overpotential η_a on the anode surface (defined as the difference of the electrode and electrolyte potentials on this surface) reaches zero. A laterally infinite-cell model was used in these calculations. The C-rate of the charge is indicated in panel a (1C = 2.37 mA/cm^2 at 30 °C). When the overpotential η_a becomes negative, Li plating is thermodynamically favored, competing with Li intercalation into graphite. At a C-rate below 2C, the condition is not met even at full lithiation. As the porosity decreases, the lithium diffusion resistance in the electrolyte within the separator increases, the cell and the anode become polarized, so the zero overpotential is reached at a lower charge. When the porosity ϵ decreases to 0.1, Li begins to plate at 10% charge. The curves become steep for low currents predicting the attainment of Li plating condition for ϵ<0.2, which corresponds to 50% pore closure in an ϵ=0.4 separator.

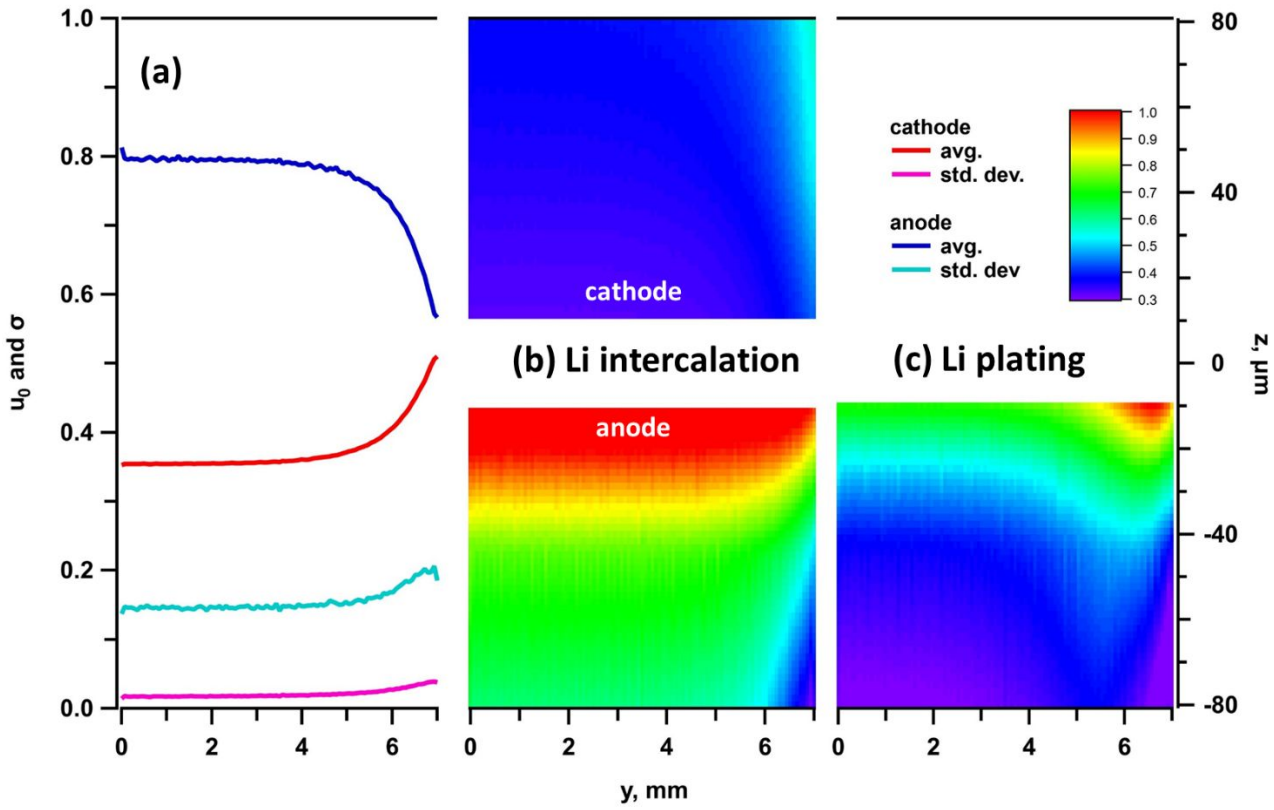

Figure 10. (a) The z-average u_0 and standard deviation σ for lithiation of the electrodes in a model cylindrical cell (a single-phase solid solution model with 5-layer particles of the active material). The distribution is obtained at the end of 6C charge to 2.3 mAh/cm^2 (at which the cell voltage is 4.5 V) assuming variable porosity in the separator (ϵ_0 = 0.4, Ξ = 0.75). The characteristic "flat top" shape is obtained in the interior, and there is rapid variation near the edges resembling the ones observed in Figure 8b. Panel b shows false-color lithiation map for the electrodes with the color sale given on the right. Panel c shows end-of-charge Li plating currents across the anode matrix. The maximum currents are observed outside of the flat top inner region but away from the edge.

Notes and references

1. V. Murray, D. S. Hall and J. R. Dahn, *J. Electrochem. Soc.*, 2019, **166**, A329-A333.
2. B. R. Long, S. G. Rinaldo, K. G. Gallagher, D. W. Dees, S. E. Trask, B. J. Polzin, A. N. Jansen, D. P. Abraham, I. Bloom, J. Bareño and J. R. Croy, *J. Electrochem. Soc.*, 2016, **163**, A2999-A3009.
3. S. Chen, C. Niu, H. Lee, Q. Li, L. Yu, W. Xu, J.-G. Zhang, E. J. Dufek, M. S. Whittingham, S. Meng, J. Xiao and J. Liu, *Joule*, 2019, **3**, 1094-1105.
4. G. Y. Gor, J. Cannarella, C. Z. Leng, A. Vishnyakov and C. B. Arnold, *J. Power Sources*, 2015, **294**, 167-172.
5. J. Cannarella, X. Liu, C. Z. Leng, P. D. Sinko, G. Y. Gor and C. B. Arnold, *J. Electrochem. Soc.*, 2014, **161**, F3117-F3122.
6. K. P. C. Yao, J. S. Okasinski, K. Kalaga, I. A. Shkrob and D. P. Abraham, *Energy Environ. Sci.*, 2019, **12**, 656-665.
7. K. P. C. Yao, J. S. Okasinski, K. Kalaga, J. D. Almer and D. P. Abraham, *Adv. Energy Mater.*, 2019, **9**, 1803380.
8. D. P. Finegan, A. Quinn, D. S. Wragg, A. M. Colclasure, X. Lu, C. Tan, T. M. M. Heenan, R. Jervis, D. J. L. Brett, S. Das, T. Gao, D. A. Cogswell, M. Z. Bazant, M. D. Michiel, S. Checchia, P. R. Shearing and K. Smith, *Energy Eviron. Sci*, 2020, DOI: 10.1039/d1030ee01191f.
9. S. R. Daemi, C. Tan, A. Vamvakeros, T. M. M. Heenan, D. P. Finegan, M. D. Michiel, A. M. Beale, J. Cookson, E. Petrucco, J. S. Weaving, S. Jacques, R. Jervis, D. J. L. Brett and P. R. Shearing, *Energy Environ. Sci.*, 2020, **13**, DOI: 10.1039/d1030cp01851a.
10. D. P. Finegan, A. Vamvakeros, C. Tan, T. M. M. Heenan, S. R. Daemi, N. Seitzman, M. D. Michiel, S. Jacques, A. M. Beale, D. J. L. Brett, P. R. Shearing and K. Smith, *Nature Comm.*, 2020, **11**, 631.
11. J. Cannarella and C. B. Arnold, *J. Electrochem. Soc.*, 2015, **162**, A1365-A1373.
12. Y. Yang, R. Xu, K. Zhang, S. J. Lee, L. Mu, P. Liu, C. K. Waters, S. Spence, Z. Xu, C. Wei, D. J. Kautz, Q. Yuan, Y. Dong, Y. S. Yu, X. Xiao, H. K. Lee, P. Pianetta, P. Cloetens, J. S. Lee, K. Zhao, F. Lin and Y. Liu, *Adv. Energy Mater.*, 2019, **9**, 1900674.

13. R. Xu, Y. Yang, F. Yin, P. Liu, P. Cloetens, Y. Liu, F. Lin and K. Zhao, *J. Mech. Phys. Sol.*, 2019, **129**, 160-183.
14. A. Mistry, F. L. E. Usseglio-Viretta, A. Colclasure, K. Smith and P. P. Mukherjee, *J. Electrochem. Soc.*, 2020, **167**, 090542.
15. S. J. Harris and P. Lu, *J. Phys. Chem. C*, 2013, **117**, 648-6492.
16. I. A. Shkrob, M.-T. F. Rodrigues, D. W. Dees and D. P. Abraham, *J. Electrochem. Soc.*, 2019, **166**, A3305-A3313.
17. P. Arora, M. Doyle and R. E. White, *J. Electrochem. Soc.*, 1999, **146**, 3543-3553.
18. W. Li, H. Y. Asl, Q. Xie and A. Manthiram, *J. Am. Chem. Soc.*, 2019, **141**, 5097-5101.
19. S. P. Timoshenko and J. N. Goodier, *Theory of Elasticity*, McGraw Hill, New York, 1970.
20. A. M. Wahl, *Mechanical springs*, McGraw-Hill, New York, 1963.
21. C. Wagner, *J. Electrochem. Soc.*, 1951, **98**, 116-128.
22. M.-T. F. Rodrigues, K. Kalaga, S. E. Trask, D. W. Dees, I. A. Shkrob and D. P. Abraham, *J. Electrochem. Soc.*, 2019, **166**, A996-A1003.
23. T. R. Tanim, P. P. Paul, V. Thampy, C. Cao, H.-G. Steinruck, J. N. Weker, M. F. Toney, E. J. Dufek, M. C. Evans, A. N. Jansen, B. J. Polzin, A. R. Dunlop and S. E. Trask, *Cell Reports Phys. Sci* 2020, **1**, 100114.
24. K. G. Gallagher, D. W. Dees, A. N. Jansen, D. P. Abraham and S.-H. Kang, *J. Electrochem. Soc.*, 2012, **159**, A2029-A2037.
25. D. W. Dees, V. S. Battaglia and A. Belanger, *J. Electrochem. Soc.*, 2002, **110**, 310-320.